Author Manuscript

Author Manuscript

Author Manuscript

Author Manuscript

HHS Public Access

Author manuscript

Nexus. Author manuscript; available in PMC 2025 February 13.

Published in final edited form as:

Nexus. 2024 June 18; 1(2): . doi:10.1016/j.ynexs.2024.100016.

Transfer learning on physics-informed neural networks for tracking the hemodynamics in the evolving false lumen of dissected aorta

Mitchell Daneker[1,2,8], **Shengze Cai**[3,8], **Ying Qian**[4], **Eric Myzelev**[5], **Arsh Kumbhat**[6], **He Li**[4,*], **Lu Lu**[1,7,9,*]

[1]Department of Statistics and Data Science, Yale University, New Haven, CT 06511, USA

[2]Department of Chemical and Biomolecular Engineering, University of Pennsylvania, Philadelphia, PA 19104, USA

[3]Institute of Cyber-System & Control, College of Control Science & Engineering, Zhejiang University, Hangzhou 310058, China

[4]School of Chemical, Materials, and Biomedical Engineering, University of Georgia, Athens, GA 30602, USA

[5]Department of Mathematics, University of Pennsylvania, Philadelphia, PA 19104, USA

[6]Department of Mathematics, ETH Zurich, 8092 Zurich, Switzerland

[7]Wu Tsai Institute, Yale University, New Haven, CT 06510, USA

[8]These authors contributed equally

[9]Lead contact

Abstract

Aortic dissection is a life-threatening event that is responsible for significant morbidity and mortality in individuals ranging in age from children to older adults. A better understanding of the complex hemodynamic environment inside the aorta enables clinicians to assess patient-specific risk of complications and administer timely interventions. In this study, we propose to develop and validate a new computational framework, warm-start physics-informed neural networks (WS-PINNs), to address the limitations of the current approaches in analyzing the hemodynamics inside the false lumen (FL) of type B aortic dissection vessels reconstructed from apolipoprotein null mice infused with AngII, thereby significantly reducing the amount of required measurement data and eliminating the dependency of predictions on the accuracy and availability of the inflow/outflow boundary conditions. Specifically, we demonstrate that the WS-PINN models allow us

This is an open access article under the CC BY-NC-ND license (https://creativecommons.org/licenses/by-nc-nd/4.0/).

*Correspondence: he.li3@uga.edu (H.L.); lu.lu@yale.edu (L.L.).

AUTHOR CONTRIBUTIONS

Conceptualization, L.L. and H.L.; methodology, M.D., S.C., H.L., and L.L.; software, M.D., S.C., Y.Q., and H.L.; validation, M.D., H.L., E.M., and A.K.; writing – original draft, M.D. and H.L.; writing – review & editing, M.D., S.C., Y.Q., E.M., A.K., H.L., and L.L.; visualization, M.D. and H.L.; supervision, L.L. and H.L.

DECLARATION OF INTERESTS

The authors declare no competing interests.

Author Manuscript Author Manuscript Author Manuscript Author Manuscript

to focus on assessing the 3D flow field inside FL without modeling the true lumen and various branched vessels. Furthermore, we investigate the impact of the spatial and temporal resolutions of MRI data on the prediction accuracy of the PINN model, which can guide the data acquisition to reduce time and financial costs. Finally, we consider the use of transfer learning to provide faster results when looking at similar but new geometries. Our results indicate that the proposed framework can enhance the capacity of hemodynamic analysis in vessels with aortic dissections, with the promise of eventually leading to improved prognostic ability and understanding of the development of aneurysms.

IN BRIEF

Aortic dissection poses significant health risks across all age groups. This study introduces a new computational framework, warm-start physics-informed neural networks (WS-PINNs), to improve the hemodynamic analysis of type B aortic dissections in mice models. WS-PINNs significantly reduce the need for extensive measurement data and eliminate reliance on precise inflow/outflow boundary conditions. By focusing on the false lumen without modeling the true lumen and branched vessels, the WS-PINN models enable detailed 3D flow field assessment. We evaluate WS-PINNs on noisy examples and run an analysis on computational efficiency, finding that WS-PINNs can handle expected levels of MRI measurement noise and are generally more efficient than traditional CFD approaches, especially when using transfer learning. Importantly, WS-PINNs avoid the cumbersome preprocessing and mesh generation required by CFD. Our findings demonstrate that WS-PINNs enhance hemodynamic analysis, potentially leading to better prognostic capabilities and understanding of aneurysm development.

INTRODUCTION

Thoracic aortic dissection (AD) is a cardiovascular pathology caused by a tear or rupture in the intimal layer of the aortic wall, allowing blood to flow in and dissect the intimal and medial layer of the arterial wall.[1,2] These dissections often propagate within the media and connect with the original aortic lumen or *"*true lumen*"* (TL) to form a so-called false lumen (FL) within the aortic wall, as illustrated in Figure 1A. The dissected aortas are susceptible to rupture due to the weakened vessel wall, potentially leading to a life-threatening crisis responsible for up to 15,000 deaths per year in the United States.[3] In contrast to type A ADs, which often require urgent surgery upon diagnosis, acute type B ADs (TBADs) might either stabilize to an uncomplicated form that can be treated with optimal medical therapy or progress into a complicated form that demands immediate medical intervention,[4] including thoracic endovascular aortic repair (TEVAR) or, less frequently, open surgical repair. Although TEVAR has demonstrated its effectiveness in improving clinical outcomes by promoting aortic remodeling and FL thrombosis,[5–7] its use to patients with uncomplicated TBAD remains controversial because of excess cost and procedural risks. Since up to 65% of acute uncomplicated TBAD will eventually progress to a complicated state within 5 years, an accurate prognosis of the evolution of TBAD is essential to identify patients with a high risk of developing complications to optimize the far-reaching therapeutic consequences.[2,8]

Morphological factors of dissected aorta derived from anatomic imaging (eg, maximal thoracic aortic diameter; the initial FL size; the number, size and location of entry tears)

Author Manuscript Author Manuscript Author Manuscript Author Manuscript

have traditionally been used to assess the risk of FL growth and subsequent rupture in patients with TBAD.[9–13] Specifically, systematic studies on the morphological factors of TBAD suggest that aortas with a diameter >40 mm and an FL diameter >22 mm at diagnosis are associated with adverse events.[14] Moreover, a higher number of re-entry tears had a protective effect against FL expansion,[13,15] whereas a shorter distance between the primary tear and the left subclavian artery offspring was linked to aortic growth in uncomplicated TBAD.[16] Despite these promising findings, identifying the disease progression solely based on the geometric features is likely insufficient for prognosis. For example, previous clinical evidence showed that FL can remain patent, partially thrombosed, or fully filled with thrombus, leading to variable clinical outcomes.[17–19] Specifically, patients with completely thrombosed dissections are reported to show a better prognosis, as complete thrombosis of the residual FL might be a sign of healing and remodeling of the aortic wall, while patent and partially thrombosed FLs appear to be susceptible to further dissection or eventual rupture.[20–22] As hemodynamics plays an essential role in dictating thrombus formation, quantification of blood flow in the dissected aorta is required to assess the extent of FL thrombosis and the risk of FL rupture.

With the recent advances in magnetic resonance (MR) technology, the volumetric phase-contrast MRI, also known as four-dimensional (4D) flow MRI, has increasingly been used for hemodynamic analysis in cardiovascular diseases as it enables the quantification of three-dimensional (3D) blood flow field in the heart and large vessels.[23–33] However, its limited spatial and temporal resolutions (0.7–1.2 mm spatial and 40–80 ms temporal) and reduced effectiveness in analyzing sluggish flow compromise its performance in quantifying the hemodynamics in the near-wall region inside FL.[34–36] Other diagnostic modalities, such as ultrasound and transesophageal echocardiography, only measure partial flow data on planes or at a given point of view and thus cannot provide a complete description of the complicated 3D flow field inside FL for thrombotic propensity evaluation.[37]

However, computational fluid dynamics (CFD), which simulates the blood flow based on Navier-Stokes equations, has been broadly employed to illustrate the complex blood flow patterns in macro- and micro-blood vessels with pathological alterations.[38–45] Informed by patient-specific inflow/outflow boundary conditions (BCs), referred to as flow BCs in this study, measured by either ultrasound or MRI, CFD simulations can provide a high-resolution assessment of hemodynamics inside FL of TBAD vessels reconstructed based on computed tomography (CT) angiography imaging.[46–53] Moreover, CFD can evaluate the pressure and shear stress that are difficult to measure *in vivo*. Notwithstanding these advantages, the reliability of CFD simulations primarily depends on the patient-specific flow BCs for all the inlet and outlet vessels, as illustrated in Figure 1B, which are often not accessible due to practical and ethical constraints.

Given the lack of availability of patient-specific flow BCs to inform CFD simulation and the limited accuracy of 4D MRI in predicting FL hemodynamics and thrombogenesis, there is a pressing need to explore new data assimilation algorithms to overcome the limitations of these two approaches. Recently, scientific machine learning models, which combine measurement data with the laws of physics using neural networks (NNs), have emerged as a novel tool for solving inverse or illposed engineering problems.[54–61] In particular, physics-

Author Manuscript Author Manuscript Author Manuscript Author Manuscript

informed NNs (PINNs), which integrate Navier-Stokes equations into the loss function of the NN,[62–66] could assimilate the low-resolution patient-specific MRI data and laws of physics to the current capability of assessing hemodynamics in vessels with TBAD for better prognosis of disease progression. Several attempts[67–70] have demonstrated the feasibility of employing PINNs to inform hemodynamics within aneurysmal or stenosed channels with noisy data, sparse data, or even without measurement data. However, these prior studies only test the performance of PINNs on two-dimensional (2D) or 3D idealized geometries, which cannot characterize the complexity of the realistic patient-specific TBAD vessels. Thus, the capability and applicability of PINN models in clinical applications remain to be investigated.

In this paper, we employ warm-start PINNs (WS-PINNs), as illustrated in Figure 2, to predict hemodynamics in realistic 3D dissected aortas reconstructed from apolipoprotein null mice infused with angiotensin II (AngII),[71–73] a well-established animal model for studying the parthenogenesis and pathology of ADs. WS-PINNs are trained with data first without considering the constraints from the laws of physics to achieve faster convergence (warm-up stage). Once WS-PINNs converge, physics constraints will be imposed to enhance the interpolation among the measurement data. We demonstrate that WS-PINNs models allow us to focus only on assessing the 3D flow field inside FL without modeling the TL and various branched vessels (Figure 1C), thereby considerably reducing the amount of required measurement data and eliminating the dependency of predictions on the accuracy and availability of the flow BCs. We also systematically evaluate model performance on the temporal and spatial resolution of the measurement data (i.e., from 4D MRI), aiming to determine the minimum data acquisition from MRI scanning while preserving the accuracy of the model predictions for assessing the hemodynamic metrics associated with thrombus formation and FL evolution. Furthermore, we demonstrate that by employing transfer learning, the trained transfer learning-WS-PINNs models can be used to predict hemodynamics in the evolved FL with few new data and minimal retraining, thus reducing the expense of data acquisition in the follow-up examinations of patients with TBAD.

RESULTS

WS-PINNs provide flow field predictions comparable to the CFD simulations

Here, we examine the performance of the proposed WS-PINNs model in inferring the 3D flow field inside the FL without considering the TL and other branches of the examined three mouse geometries. We use the results of CFD as ground truth (reference) to assess the accuracy of the predictions of WS-PINNs. The spatial resolution of the MRI data used in the WS-PINNs is determined to be 39, 59, and 45 slices of data along the longitudinal direction of the aorta, while the temporal resolution is determined to be 29 snapshots per cardiac cycle for all three geometries. These selections are made based on the conservative assumption of a maximum spatial resolution of 3.0 mm and a maximum temporal resolution of 40 ms[74] on human aortas and convert to the size of mouse aortas, which are approximately 20 times smaller than the human aortas. We note that the computational domain of PINNs only includes the aneurysm (Figure 1C) without the blood vessel, and we do not have the BC at the interface between the blood vessel and the aneurysm.

Author Manuscript Author Manuscript Author Manuscript Author Manuscript

Figure 3 illustrates the prediction of the flow field on four slices along the entry of the FL of aneurysm 1, where the complex flow pattern is observed. We note that the magnitude of the w component of velocity overwhelms the other two components within the FL. As a result, the relative errors of the predictions of u and v are slightly larger than the w, particularly around the entry of the FL. This increased prediction error is likely attributed to the complex flow pattern at the connection of TL and FL, as illustrated by the flow streamline plotted at peak systole in Figure 3. In addition, as we did not consider the TL and other branch vessels in the WS-PINNs model, we did not specify the flow BC around the entry, which could also lead to a prediction error. Despite the errors around the entry, the overall model predictions are in good agreement with CFD simulation results (reference), with an L_2 relative error of 2.78%. As illustrated in the insets of Figure 3, good agreement is achieved in the region close to the vessel wall, which is essential for computing the hemodynamic metrics associated with disease progression and thrombus formation, such as wall shear stress. This finding demonstrates the capacity of WS-PINNs to infer hemodynamics within the FL of dissected aortas without prior knowledge of the inlet and outlet BCs.

Next, we examine the predictions of the flow field in the other two aneurysms, and the results are represented in Figures 4 and 5 using flow streamlines at peak systole to understand the pattern and strength of flow that might contribute to the geometries of FL and the size of its entry. The patterns of the vortical zones differ markedly in aneurysms 2 and 3, which are affected mainly by the size of the opening of the FL to the TL. The small entry of the small FL (Figure 5) leads to the smallest vortex in FL, whereas the large entry size in the large FL (Figure 4) causes the flow to break into two vortices located at the proximal and distal sites of inside the FL. These results show the significant discrepancy of flow patterns within the FL of dissected aortas. The predictions of WS-PINNs at four selected slices around the entry and the corresponding reference are plotted in the insets of Figures 4 and 5. It is noted that WS-PINNs demonstrate superior performance in capturing the key features of the complex flow pattern at the opening of FL to the TL, considering the flow BCs at the opening are not provided. The L_2 relative errors of the WS-PINNs are 2.05% and 2.71% for aneurysms 2 and 3, respectively, which are comparable to the prediction error for aneurysm 1, demonstrating the robustness of WS-PINNs for inferring hemodynamics in dissected aortas with various geometries. We also observed increased errors near the entry of the FL due to the lack of information on the flow BCs. These findings demonstrate the feasibility and capacity of WS-PINNs to infer the flow field within the FL by incorporating the sparse measurement data without the knowledge of inlet and outlet BCs.

Impact of spatial and temporal resolutions of measurement data on the accuracy of WS-PINNs predictions

In this section, we systematically examine how the spatial and temporal resolutions of measurement data impact the prediction of the WS-PINNs by gradually reducing the amount of measurement data provided to WS-PINNs for inferring the flow field. The spatial and temporal resolutions will be reduced to 80%, 60%, 40%, and 20% of the original dataset used in the last section, respectively. We use these measurement data to train a fully connected neural network (FNN) without incorporating the laws of physics into the loss function of the FNN. L_2 relative error of the predictions of the velocity magnitude with

Author Manuscript Author Manuscript Author Manuscript Author Manuscript

respect to various numbers of slices and snapshots for the three examined aneurysms are summarized in Figure 6A. These three panels show a notable trend of increases in prediction errors as the spatial and temporal resolutions are reduced. In particular, the increases in error are more pronounced for aneurysms 1 and 3 compared to aneurysm 2. This discrepancy is likely attributed to the different shapes of the FL. As illustrated in Figure 1C, the shape alterations of aneurysms 1 and 3 along the direction of the aorta are more significant, leading to more drastic flow field changes that require more measurement data to infer the 3D flow field within the FL. Conversely, aneurysm 2 exhibits a more uniform shape, as indicated by comparable cross-sectional areas along the longitudinal axis of the aorta. As a result, the flow patterns within the FL are less variable, leading to a reduction in the amount of data necessary for reconstructing the hemodynamics inside the FL.

Next, we predict the flow field within the FL by integrating the laws of physics into the loss function of the FNN. The resultant L_2 relative error of the predictions of the velocity magnitude with respect to various numbers of slices and snapshots for the three examined aneurysms are summarized in Figure 6B, where we observe no notable improvement for predictions in case of high spatial and temporal resolutions. As for the predictions based on relatively low spatial and temporal resolutions, the errors have been greatly reduced after the laws of physics are considered, demonstrating the significant role of the laws of physics in facilitating the interpolation of the flow velocities within regions without measurement data. The average reductions in the prediction errors for aneurysms 1–3 are 34%, 30%, and 38%, respectively. These results indicate the superior capability of WS-PINNs in inferring the hemodynamics within the FL than NNs, particularly in cases where the measurement data are sparse in spatial and temporal spaces. We also note in Figure 6C, which depicts the relative difference described in Equation 1,

$$\text{Relative Difference} = \frac{\mathrm{L}_{2_{\text{data only}}} - \mathrm{L}_{2_{\text{ws-PINN}}}}{\mathrm{L}_{2_{\text{data only}}}} \quad \text{(Equation 1)}$$

that for aneurysms 1 and 3, the error escalates more rapidly when the temporal resolution is decreased solely compared to the scenario where only the spatial resolution is reduced. In contrast, the predictions for aneurysm 2 are more sensitive to the temporal resolution. This difference is probably linked to the more complex flow patterns within aneurysms 1 and 3 that demand a greater amount of measurement data to accurately capture the complete flow patterns within the fluid domain, while the more uniform flow inside aneurysm 2 requires less measurement data.

Performance of WS-PINNs on processing noisy data

The 4D flow MRI data acquired from clinics often is contaminated by measurement noise originating from various sources such as imperfections in the imaging equipment, motion artifacts, and other environmental factors. To allow for a more realistic representation of 4D flow MRI data, we modified the velocity data by introducing Gaussian white noise with an SD denoted as α to simulate the measurement noise inherent in MRI data. The added noise is relative to the largest velocity value and thus has a more significant impact on low-velocity

Author Manuscript Author Manuscript Author Manuscript Author Manuscript

data. The parameter α is adjusted within the range of 0%–25%, reflecting different degrees of acquisition noise associated with MRI scan data, as informed by earlier experimental evaluations.[75,76] The impact of the noise on the L_2 relative errors of predictions of $\|\mathbf{v}\|$ is summarized in Figure 7. Each noise level was run three times, and error bars indicate SDs of the predictions. We consider two resolution cases in aneurysm 1, one at the maximum resolution and one at 60% spatial and temporal resolution, denoted as high and medium, respectively. For both resolutions, we compare the data only and WS-PINNs models.

At 5% noise, the high-resolution cases nearly double their L_2 relative errors, with an average 127% increase for data only and an 82% increase for WS-PINNs. The medium resolution errors for data only and WS-PINNs increase by 28% and 38%, respectively. As the noise level increases, the high-resolution models grow at nearly the same rate, seeing WS-PINNs remain at an average of 39% lower L_2 relative error. Compared to the initial error reduction of 24%, WS-PINNs have an obvious advantage over data-driven methods for this case. Considering the medium resolution, the error difference decreased at 15% noise, but this seems an outlier as the other four noise levels see lower errors on the order of 77%, compared to the 50% lower error at 0 noise. Overall, WS-PINNs appear more robust to noise than the standard data-driven model.

Transfer learning accelerates the training of WS-PINNs for hemodynamic predictions in evolved aneurysm geometries

Next, we consider the effect of transfer learning applied to evolved aneurysms, mimicking the growth of an aneurysm over time. Here, we use aneurysm 1 as an example and stretch the original geometry along the z-axis up to 40% of its original length with an increment of 10%. The new geometries will be solved via CFD to serve as ground truth for comparison with the predictions of WS-PINNs. Transfer learning is conducted by loading the previous model's weights and biases into the model before training for the new geometries begins. We propose the dubbed boundary warmup strategy to ensure that the previous model was prepared appropriately for the new stretched boundary, as discussed in the section "transfer learning WS-PINNs." Once the boundary warmup is completed, it is found that the data warmup stage converges much more quickly, on the order of 10,000 iterations, as opposed to the 20,000–50,000 required for WS-PINNs. Finally, the transfer learning-WS-PINNs training time is shortened from 20,000 to 50,000 iterations required for WS-PINNs to 3,000 to 5,000 iterations. Figures 8A and 8B depict the difference in iterations and errors for different resolutions in aneurysms with varying extents of FL evolution, and Figure 8 summarizes the prediction errors for cases with/without using transfer learning. It is noted that the speedup is significant, with more than 20,000 fewer iterations required for training with transfer learning-WS-PINNs than that of WS-PINNs. In particular, the majority of these iterations occur at the more computationally costly stage, where both data and the laws of physics are considered in training. As a result, the employment of transfer learning reduces the overall computational time by 50% for high resolutions and upward to 80% for low-resolution cases when comparing the time for training WS-PINNs from scratch.

Author Manuscript Author Manuscript Author Manuscript Author Manuscript

DISCUSSION

4D MRI has been used increasingly to assess hemodynamics inside dissected aortas, but its limited spatial and temporal resolutions compromise its effectiveness in analyzing the blood flow within FL. CFD can provide an accurate estimation of the hemodynamics inside dissected aortas, but the accuracy of CFD simulations relies on the knowledge of the patient-specific BCs at all inlet and outlet vessels, which are often unavailable in clinical practice. In this study, we have proposed a new computational framework that can incorporate low-resolution MRI data and leverage the laws of physics for fluid mechanics to address these issues. In contrast to the conventional CFD simulations, WS-PINNs do not require patient-specific flow BCs to infer the high-resolution 3D flow field thanks to the superior capability of PINNs for solving inverse and ill-posed problems in fluid dynamics. WS-PINNs only require knowledge of partial MRI measurements at regions of interest (i.e., velocities on the transverse planes along the dissected aortas [Figure 1C]) to resolve flow fields, thereby significantly reducing the time for processing the data for entire aortas. In particular, we show that the WS-PINNs can characterize the flow within the FL of the dissected aorta without mesh generation and knowledge of flow BCs, thus overcoming the challenges encountered by conventional CFD simulations. Here, we note the interdisciplinary nature of this study as constructing the WS-PINNs requires significant effort from data science and machine learning domain experts, while data measurements need to be performed by biomedical engineers (synthetic data) or radiologists (MRI data). The final clinical decision will be made by cardiovascular surgeons.

The training process of WS-PINN and transfer learning-WS-PINN involves gradually providing various pieces of knowledge (Figure 9) to the PINN in a certain order to achieve better results rather than using PINN directly. This process is similar to that used by Xu et al.,[77] in which different rules are automatically adjusted for embedding order based on importance. In addition to reconstructing the 3D flow field based on sparse measurement data, WS-PINNs are proficient in handling measurement noise by integrating the laws of physics into the loss function, which is a feature critical to process clinical data characterized by measurement noise. Integration with physical models in the WS-PINNs can also loosen the requirements of MRI data acquisitions, reducing the time and financial cost of MRI scanning. Specifically, in the case of FL with drastic shape changes, the model predictions are more sensitive to the spatial resolution of the measurements, while the prediction errors are more dependent on the temporal resolution for FL, with more uniform shapes. As a result, the proposed WS-PINNs model can guide data acquisition from MRI scanning while preserving the accuracy of the model predictions for assessing the hemodynamic metrics associated with thrombus formation and FL evolution.

Computational efficiency is vital for gauging the practical implications of our PINN approach. PINN training was run on one NVIDIA GeForce RTX 3090 graphics processing unit. The average training time and SD over all three aneurysms for WS-PINN is 21.61 ± 0.32 min, and for transfer learning-WS-PINN, it is 10.32 ± 0.40 min. As a comparison, CFD simulations were run on one Intel Xeon Gold 6230 central processing unit by using 32 threads. CFD runtimes have greater variability across three aneurysms. CFD simulations on aneurysm 1 took 15.26 min, 85.35 min on aneurysm 2, and 63.33 min on aneurysm

Author Manuscript Author Manuscript Author Manuscript Author Manuscript

3. The variance in CFD runtime stems from differences in the generated meshes among the three aneurysms. While WS-PINN is slower than CFD in aneurysm 1, our method is faster for the other two aneurysms and has more consistent runtimes. Additionally, transfer learning-WS-PINNs are faster than their CFD counterparts for all three cases. It is important to note that the provided runtimes do not include the extensive time for pre-processing and mesh generation in CFD—at least a few hours for a trained CFD researcher.

It is also noted that WS-PINNs provide an alternate way of storing hemodynamic data in NNs to boost storage capacity and promote data sharing. Hemodynamics analysis of dissected aortas using 4D MRI or CFD simulations involves generating a massive amount of data from either volumetric data scanned for 4D MRI or the velocity data computed on the high-density mesh. For example, data obtained from CFD simulations for one cardiac cycle for one geometry of the dissected aorta is approximately 10 GB. Such large data pose significant challenges to data transport and sharing for large cohort studies. The employment of WS-PINNs enables the storage of hemodynamic data in light-weighted NNs, which occupy less than 900 kB after compression, facilitating the model transport and sharing on Open Data Hub to reproduce the simulation results. This critical feature could significantly promote large cohort studies of the association of geometric and hemodynamic factors with the disease progression of patients with aortic aneurysms and AD.

We note several limitations of the current work. While we have successfully demonstrated the effectiveness of WS-PINNs in synthetic data generated on multiple realistic geometries, their accuracy and efficiency in real flow MRI data remain an area requiring additional investigations. Real clinical data can introduce complexities and variations that may impact the model performances compared to the controlled *in vitro* or synthetic data. Further research and development efforts along these lines will be essential to harness the full potential of WS-PINNs. In addition, the suitability and practicality of the proposed framework are demonstrated by utilizing a model of mouse AD in current research. Nevertheless, the proposed method will be equally applicable to predict the hemodynamics of other dissections, artery stenosis, and diverse aneurysms. As long as the development of the alterations of vessel geometries and partial information of the hemodynamics can be measured, they can be seamlessly integrated into the WS-PINNs framework for a 3D full-flow field assessment. The proposed method represents a robust and adaptable framework that can leverage artificial intelligence-based models to merge the laws of physics with multi-modal *in vivo* data (i.e., CT and MRI), thus improving personalized prognosis for patients with TBAD or other aortic diseases.

Conclusion

Despite recent technical developments, surgery on the thoracic aorta remains challenging and is associated with significant mortality and morbidity. Decisions about when and whether to operate are based on a balance between surgical risk and the hazard of aortic rupture. These decisions are sometimes difficult in elective cases of thoracic aortic diseases, including aneurysms and dissections. Abnormal hemodynamics derived from the deterioration of the aortic wall influences disease progression. In this study, we propose developing and validating a new computational framework, WS-PINNs, to address the

Author Manuscript Author Manuscript Author Manuscript Author Manuscript

limitations of the current approaches in analyzing the hemodynamics in dissected aortas. WS-PINNs are trained with data first without considering the constraints from the laws of physics to achieve faster convergence (warm-up stage). Once WS-PINNs converge, physics constraints are imposed to enhance the interpolation among the measurement data.

Using apolipoprotein null mice as a disease model, we demonstrate the effectiveness and efficiency of WS-PINNs through the following four aspects: (1) We systematically examine the performance of the PINN model in inferring the hemodynamics inside FL of dissected aortas and demonstrate that PINN models allow us to focus only on assessing the 3D flow field inside FL without modeling the TL and various branched vessels, thereby considerably reducing the amount of required measurement data and eliminating the dependency of predictions on the accuracy and availability of the flow BCs. (2) We investigate the impact of the spatial and temporal resolutions of the measurement data on the model performance. (3) We utilize transfer learning to the trained WS-PINN models to track and record patient-specific hemodynamics data during disease progression, thus reducing the measurement data acquired for the follow-up examinations. (4) Our results show that employing PINNs for hemodynamic data storage can significantly decrease the storage demands associated with saving the massive amount of data generated from either volumetric data scanned for 4D MRI or the velocity data computed on the high-density mesh, thereby boosting storage capacity and promote data sharing for large cohort studies.

In summary, our results show that the proposed computational framework can enhance the capacity of hemodynamics analysis in TBAD, with the promise of eventually leading to improved prognostic ability and interventional planning. Furthermore, the proposed computational framework can be equally applicable to other aortic diseases, such as artery stenosis and diverse aneurysms, and thus could have a much broader impact.

Data and methods

Geometries of AD

The geometries of examined dissected aortas were extracted from apolipoprotein null mice undergoing standard subcutaneous infusion of AngII at a rate of 1,000 ng/kg/min.[71–73] The computational domains for blood flow simulations (Figure 1A) were reconstructed using combined 3D ultrasound and optical coherence tomography (OCT), while the flow BCs at the inlet, outlet, and four branches of the aorta were measured by pulsed-wave Doppler and anatomic 3D ultrasound (Figure 1B). These BCs will inform the CFD simulations, as introduced in the next section. As illustrated in Figure 1C, we employ WS-PINNs to predict the full 3D velocity field within the FL of three dissected aortas—one with a medium-size FL (left), one with a large-size FL (center), and one with a small-size FL (right)—based on the sparse cross-sectional velocities data without considering the TL and multiple branch outlets. More detailed information about the experiments and geometry reconstruction process can be found in the prior work of Phillips et al.[72] and Bersi et al.[78]

To mimic the growth of the dissecting aneurysm during the progression of TBAD, we alter aneurysm 1 by stretching the original geometry along the z-axis up to 40% of its original

Author Manuscript Author Manuscript Author Manuscript Author Manuscript

length, with an increment of 10%. These new geometries are solved via CFD to serve as ground truth for comparison with the predictions of WS-PINNs.

CFD simulation for data generation for training and testing WS-PINNs

We perform CFD simulations to generate data for training and testing the proposed WS-PINNs. We utilize the incompressible velocity-pressure form of the Navier-Stokes equation and the incompressible continuity equation

$$\rho\left[\frac{\partial \mathbf{V}}{\partial t} + (\mathbf{V} \cdot \nabla \mathbf{V})\right] = -\nabla p + \mu \nabla^2 \mathbf{V}, \quad \text{(Equation 2)}$$

$$\nabla \cdot \mathbf{V} = 0, \quad \text{(Equation 3)}$$

where t is time, $\mathrm{V}(x,t) = [u, v, w]^T$ is the velocity vector, $p(x,t)$ is the pressure field, $x \in \Omega$ is the spatial coordinate, ρ is the density of the fluid, and μ is the dynamic viscosity of the fluid. The blood is assumed to be an incompressible Newtonian fluid with a density of 1,050 kg/m^3 and dynamic viscosity of 3.675×10^{-3} Pa s.

The flow BCs used in the CFD simulations are illustrated in Figure 1B, where the mouse-specific inlet flow rate waveforms are prescribed at the level of the proximal suprarenal aorta as a Dirichlet BC using a Womersley velocity profile[79] following pulsed-wave (PW) Doppler measurements taken at the same location.[72] Two-parameter (also known as RC) Windkessel models match PW Doppler measurements in the major outlet vessels.[80] Taking advantage of flow waveforms at the outlets, we compute time-dependent R(t)C values to reproduce the flow waveforms more effectively. A zero-flux Neumann BC for velocity was considered at each outlet. More detailed information on the calculation of the inlet and outlet BCs can be found in our prior work.[81] Additionally, the CFD simulations consider the no-slip BC at the vessel walls. We solve Equations 2 and 3 using the open-source, parallel CFD code NEKTAR.[82] We have generated 20 time frames per cardiac cycle from CFD simulations and extract the velocity data from each time frame by using point clouds with a uniform grid of 0.7-mm spacings projected into multiple planes based on the temporal and spatial resolutions of the MRI measurements. Three velocity images are created for each time frame, representing three velocity components: V_x, V_y, and V_z. The CFD simulation results are used as ground truth to examine the performance of the proposed WS-PINNs models as well as in the generation of the MRI data used by our PINN models, which is represented as 2D slices of velocity data across the different snapshots.

PINNs

As illustrated in Figure 2A, the employed PINN model takes four variables as inputs, consisting of three spatial components $[x, y, z]$ and one temporal component t, and outputs three components of the velocity $[u, v, w]$ and the pressure $[p]$. To facilitate the training of the NN, all input variables are scaled to −1 and 1 based on the geometry of the dissected

Author Manuscript Author Manuscript Author Manuscript Author Manuscript

aorta and simulation time before being input into networks. The NN in WS-PINNs consists of 8 hidden layers with a width of 128. We use the Adam optimizer in all training stages with a learning rate of 10^{-3} for data only and 10^{-4} for PINN. Step decay is used with a decay rate of 0.5 and step size of 10,000. The sin activation function is used, and network parameters are initialized using the Xavier scheme. Here, we choose the sin activation function as it is a periodic activation function that helps model the oscillatory nature of the Womersley velocity profile. This approach was successfully implemented by Wang et al.[83] to model partial differential equation (PDE) systems with a periodic nature. Additionally, it is a continuously differentiable function that facilitates the computation of derivatives for evaluating the PDE residual required for computing the loss function.

It is noted that the loss function of the PINN model (Figure 2A) comprises three terms: (1) no-slip BCs on the walls of the dissected aortas whose geometry was gathered from 3D ultrasound and OCT; (2) the synthetic MRI measurement data; and (3) the laws of physics, including the Navier-Stokes and continuity equations, in the form of PDEs. When training our models, the no-slip BC on the boundary of the dissected aortas and the synthetic MRI measurement data are considered to be the supervised data, whereas the PDE residuals behave like a regularization term that ensures the model is physically constrained by the governing equations and prevents overfitting. In particular, incorporating these PDEs into the loss function of the network enhances the interpolation capability of PINNs when making predictions in the regions between the available MRI data. As a result, the total loss of our PINN models is defined as

$$\mathscr{L}(\boldsymbol{\theta}) = \mathscr{L}^{pde}(\boldsymbol{\theta}) + \mathscr{L}^{bc}(\boldsymbol{\theta}) + \mathscr{L}^{data}(\boldsymbol{\theta}),$$

where $\boldsymbol{\theta}$ is the parameters of the network. We consider N^{pde} points in the dissected aorta domain, with corresponding network predictions $[u, v, w, p]$ represented as $\mathscr{T}^{pde}$.$\mathscr{L}^{pde}$ represents the loss computed from the employed PDEs and can be expressed by

$$\mathscr{L}^{pde}(\boldsymbol{\theta}) = \frac{1}{\left|\mathscr{T}^{pde}\right|}\sum_{(x,t)\in\mathscr{T}^{pde}}\Big(w^{pde_1}\mathscr{L}^{pde_1} + w^{pde_2}\mathscr{L}^{pde_2} + w^{pde_3}\mathscr{L}^{pde_3} + w^{pde_4}\mathscr{L}^{pde_4}\Big)|_{(x,t)},$$

where

$$\mathscr{L}^{pde_1} = \left(\frac{\partial u}{\partial x} + \frac{\partial v}{\partial y} + \frac{\partial w}{\partial z}\right)^2,$$

$$\mathscr{L}^{pde_2} = \left[\rho\left(\frac{\partial u}{\partial t} + u\frac{\partial u}{\partial x} + v\frac{\partial u}{\partial y} + w\frac{\partial u}{\partial z}\right) + \frac{\partial p}{\partial x} - \mu\frac{\partial^2 u}{\partial^2 x} + \frac{\partial^2 u}{\partial^2 y} + \frac{\partial^2 u}{\partial^2 z}\right)\right]^2,$$

Author Manuscript Author Manuscript Author Manuscript Author Manuscript

$$\mathscr{L}^{pde_3} = \left[\rho\left(\frac{\partial v}{\partial t} + u\frac{\partial v}{\partial x} + v\frac{\partial v}{\partial y} + w\frac{\partial v}{\partial z}\right) + \frac{\partial p}{\partial y} - \mu\frac{\partial^2 v}{\partial^2 x} + \frac{\partial^2 v}{\partial^2 y} + \frac{\partial^2 v}{\partial^2 z}\right)\right]^2,$$

$$\mathscr{L}^{pde_4} = \left[\rho\left(\frac{\partial w}{\partial t} + u\frac{\partial w}{\partial x} + v\frac{\partial w}{\partial y} + w\frac{\partial w}{\partial z}\right) + \frac{\partial p}{\partial z} - \mu\frac{\partial^2 w}{\partial^2 x} + \frac{\partial^2 w}{\partial^2 y} + \frac{\partial^2 w}{\partial^2 z}\right)\right]^2.$$

$\mathscr{L}^{bc}$ represents the loss contributed from the no-slip BCs at N^{bc} points on the boundary, $\mathscr{T}^{bc}$. Boundary loss can be computed as

$$\mathscr{L}^{bc}(\boldsymbol{\theta}) = w^{bc}\frac{1}{|\mathscr{T}^{bc}|}\sum_{(x,t)\in\mathscr{T}^{bc}}\left(u^2 + v^2 + w^2\right)\Big|_{(x,t)}.$$

There are N^{MRI} MRI measurement data with values $\left[u^{MRI}, v^{MRI}, w^{MRI}\right]$, denoted by $\mathscr{T}^{MRI}$. $\mathscr{L}^{data}$ denotes the discrepancies between the model predictions, and it is computed by

$$\mathscr{L}^{data}(\boldsymbol{\theta}) = w^{data}\frac{1}{|\mathscr{T}^{MRI}|}\sum_{(x,t)\in\mathscr{T}^{MRI}}\Big((u_{MRI} - u)^2 + (v_{MRI} - v)^2 + (w_{MRI} - w)^2\Big)\Big|_{(x,t)}.$$

The weights $(w^{pde_1}, w^{pde_2}, w^{pde_3}, w^{pde_4}, w^{bc}, w^{data})$ are used to adjust the contributions from different loss terms such that their impact on the total loss function of the network would be of the same order of magnitude. The continuity equation is weighted at 10. Other terms are weighted at 1, except for the z-axis velocity (w) terms, which are at a higher order of magnitude and set to a weight of 0.2 to compensate. Scaling, losses, and training procedures for WS-PINNs and transfer learning-WS-PINNs are depicted in Figure 9.

WS-PINNs

The training procedure of the proposed WS-PINNs models is divided into two stages. The network is trained using only synthetic MRI data without considering the constraints from the laws of physics for 20,000–50,000 iterations. We call this step “data warm-up.” By completing the data-warming step, the network converges more quickly, as the derivatives and additional loss terms do not need to be computed while simultaneously nearing the solution provided by the data. The range of iterations is dependent on the dataset. For cases with very low resolution, it was found that more iterations are required due to initial overfitting, which is corrected as the network trains. For higher-resolution cases, too much training can lead to overfitting, compromising PINN performance in the second step. Once the network is trained on the data and warmed up, we add the physics losses. Next, the network is trained with MRI data and the laws of physics. We confirm that the network

Author Manuscript Author Manuscript Author Manuscript Author Manuscript

has converged by visually analyzing the loss function. Convergence occurs between another 20,000 and 50,000 iterations.

Transfer learning-WS-PINNs

For stretched cases where transfer learning is employed, the two-stage learning process described in the previous section is not sufficient. Although our algorithms will optimize the initial geometry, when trying to employ transfer learning with new geometry, there is no guarantee that the solution outside our original geometry can provide useful hemodynamics information since that region was not trained on. Thus, we propose an additional step before the data warm-up called “boundary warm-up” occurs, where we first let the model learn the difference in the boundaries between the old and new geometries. Specifically, we add training points sampled from the area, differentiating the old and new geometries to the BC loss. Then, we use a copy of the model trained on the original geometry and resume training the entire model using the new BCs and the old MRI data. This ensures that the area outside the initial geometry is zero and prepares said area for training. A detailed graphic of boundary warm-up is provided in Figure 9. It was found that 3,000 iterations are long enough for transfer learning-WS-PINNs to learn this boundary difference, which is evident from a desired error comparable to the standard WS-PINNs.

EXPERIMENTAL PROCEDURES

Resource availability

Lead contact—Further information and requests for resources should be directed to and will be fulfilled by the lead contact, Lu Lu (lu.lu@yale.edu).

Materials availability—This study did not generate unique materials.

Data and code availability—The data and code for this work is publicly available on the GitHub repository: https://github.com/lu-group/pinn-thrombus-mri.

ACKNOWLEDGMENTS

H.L. and L.L. gratefully acknowledge the helpful discussion with Dr. Bradley G. Leshnower from Emory University School of Medicine. H.L. thanks Dr. Xiaoyun Xu from Imperial College London for the helpful communication.

REFERENCES

1. Egbe AC, Crestanello J, Miranda WR, et al. (2019). Thoracic aortic dissection in tetralogy of fallot: a review of the national inpatient sample database. J. Am. Heart Assoc. 8, e011943. [PubMed: 30871391]
2. Carrel T, Sundt TM, von Kodolitsch Y, et al. (2023). Acute aortic dissection. Lancet 401, 773–788. [PubMed: 36640801]
3. Amoah J (2023). Trend of aortic dissection mortality in USA (1999–2020). J. Am. Coll. Cardiol. 81, 2051.
4. Nienaber CA, and Clough RE (2015). Management of acute aortic dissection. Lancet 385, 800–811. [PubMed: 25662791]

Author Manuscript Author Manuscript Author Manuscript Author Manuscript

5. Jan B, Kasprzak P, Verhoeven E, et al. (2014). Endovascular repair of acute uncomplicated aortic type B dissection promotes aortic remodelling: 1 year results of the adsorb trial. Eur. J. Vasc. Endovasc. Surg. 48, 285–291. [PubMed: 24962744]
6. Nienaber CA, Divchev D, Palisch H, et al. (2014). Early and late management of type B aortic dissection. Heart 100, 1491–1497. [PubMed: 25092877]
7. Lou X, Chen EP, Duwayri YM, et al. (2023). Early results of thoracic endovascular aortic repair for the management of acute uncomplicated type B aortic dissection. Semin. Thorac. Cardiovasc. Surg. 35, 289–297. [PubMed: 35189330]
8. Juraszek A, Czerny M, and Rylski B (2022). Update in aortic dissection. Trends Cardiovasc. Med. 32, 456–461. [PubMed: 34411744]
9. Evangelista A, Galuppo V, Gruosso D, et al. (2014). Role of entry tear size in type B aortic dissection. Ann. Cardiothorac. Surg. 3, 403–405. [PubMed: 25133104]
10. Lobato AC, and Puech-Leão P (1998). Predictive factors for rupture of thoracoabdominal aortic aneurysm. J. Vasc. Surg. 27, 446–453. [PubMed: 9580243]
11. Onitsuka S, Akashi H, Tayama K, et al. (2004). Long-term outcome and prognostic predictors of medically treated acute type B aortic dissections. Ann. Thorac. Surg. 78, 1268–1273. [PubMed: 15464484]
12. Song J-M, Kim S-D, Kim J-H, et al. (2007). Long-term predictors of descending aorta aneurysmal change in patients with aortic dissection. J. Am. Coll. Cardiol. 50, 799–804. [PubMed: 17707186]
13. Evangelista A, Salas A, Ribera A, et al. (2012). Long-term outcome of aortic dissection with patent false lumen: predictive role of entry tear size and location. Circulation 125, 3133–3141. [PubMed: 22615344]
14. Spinelli D, Benedetto F, Donato R, et al. (2018). Current evidence in predictors of aortic growth and events in acute type B aortic dissection. J. Vasc. Surg. 68, 1925–1935.e8. [PubMed: 30115384]
15. Loewe C, Czerny M, Sodeck GH, et al. (2012). A new mechanism by which an acute type B aortic dissection is primarily complicated, becomes complicated, or remains uncomplicated. Ann. Thorac. Surg. 93, 1215–1222. [PubMed: 22402280]
16. Codner JA, Lou X, Duwayri YM, et al. (2019). The distance of the primary intimal tear from the left subclavian artery predicts aortic growth in uncomplicated type B aortic dissection. J. Vasc. Surg. 69, 692–700. [PubMed: 30292615]
17. Li D, Ye L, He Y, et al. (2016). False lumen status in patients with acute aortic dissection: a systematic review and meta-analysis. J. Am. Heart Assoc. 5, e003172. [PubMed: 27166218]
18. Golledge J, and Eagle KA (2008). Acute aortic dissection. Lancet 372, 55–66. [PubMed: 18603160]
19. Wu J, Song J, Li X, et al. (2021). Is partially thrombosed false lumen really a predictor for adverse events in uncomplicated type B aortic dissection: A systematic review and meta-analysis? Front. Cardiovasc. Med. 8, 788541. [PubMed: 35118140]
20. Tsai TT, Evangelista A, Nienaber CA, et al. (2007). Partial thrombosis of the false lumen in patients with acute type B aortic dissection. N. Engl. J. Med. 357, 349–359. [PubMed: 17652650]
21. Trimarchi S, Tolenaar JL, Jonker FHW, et al. (2013). Importance of false lumen thrombosis in type B aortic dissection prognosis. J. Thorac. Cardiovasc. Surg. 145, S208–S212. [PubMed: 23260434]
22. Bernard Y, Zimmermann H, Chocron S, et al. (2001). False lumen patency as a predictor of late outcome in aortic dissection. Am. J. Cardiol. 87, 1378–1382. [PubMed: 11397357]
23. Jarral OA, Tan MKH, Salmasi MY, et al. (2020). Phase-contrast magnetic resonance imaging and computational fluid dynamics assessment of thoracic aorta blood flow: a literature review. Eur. J. Cardio. Thorac. Surg. 57, 438–446.
24. Hector W. de B., Shah DJ, Patel AP, et al. (2019). Four-dimensional flow cardiovascular magnetic resonance in aortic dissection: Assessment in an ex vivo model and preliminary clinical experience. J. Thorac. Cardiovasc. Surg. 157, 467–476. [PubMed: 30121136]
25. Kari FA, Kocher N, Beyersdorf F, et al. (2015). Four-dimensional magnetic resonance imaging-derived ascending aortic flow eccentricity and flow compression are linked to aneurysm morphology. Interact. Cardiovasc. Thorac. Surg. 20, 582–588. [PubMed: 25636325]

Author Manuscript Author Manuscript Author Manuscript Author Manuscript

26. Ma LE, Markl M, Chow K, et al. (2019). Aortic 4D flow MRI in 2 minutes using compressed sensing, respiratory controlled adaptive k-space reordering, and inline reconstruction. Magn. Reson. Med. 81, 3675–3690. [PubMed: 30803006]
27. Kelly J, Pruijssen JT, Son AY, et al. (2020). Parametric hemodynamic 4D flow MRI maps for the characterization of chronic thoracic descending aortic dissection. J. Magn. Reson. Imag. 51, 1357–1368.
28. Oechtering TH, Hons CF, Sieren M, et al. (2016). Time-resolved 3-Dimensional magnetic resonance phase contrast imaging (4D flow mri) analysis of hemodynamics in valve-sparing aortic root repair with an anatomically shaped sinus prosthesis. J. Thorac. Cardiovasc. Surg. 152, 418–427. [PubMed: 27423836]
29. Burris NS, and Hope MD (2015). 4D flow MRI applications for aortic disease. Magn. Reson. Imag. Clin. N. Am. 23, 15–23.
30. Pirola S, Guo B, Menichini C, et al. (2019). 4-d flow mri-based computational analysis of blood flow in patient-specific aortic dissection. IEEE Trans. Biomed. Eng. 66, 3411–3419. [PubMed: 30872222]
31. Nakaza M, Matsumoto M, Sekine T, et al. (2022). Dual-venc 4D flow MRI can detect abnormal blood flow in the left atrium that potentially causes thrombosis formation after left upper lobectomy. Magn. Reson. Med. Sci. 21, 433–443. [PubMed: 33790138]
32. Fraser MC, Kozor R, Sherrah AG, et al. (2016). Use of multi-velocity encoding 4D flow MRI to improve quantification of flow patterns in the aorta. J. Magn. Reson. Imag. 43, 352–363.
33. Azarine A, Garçon P, Stansal A, et al. (2019). Four-dimensional flow mri: principles and cardiovascular applications. Radiographics 39, 632–648. [PubMed: 30901284]
34. Zhuang B, Sirajuddin A, Zhao S, et al. (2021). The role of 4D flow MRI for clinical applications in cardiovascular disease: current status and future perspectives. Quant. Imag. Med. Surg. 11, 4193–4210.
35. Wang Q, Guo X, Brooks M, et al. (2022). MRI in CFD for chronic type b aortic dissection: Ready for prime time? Comput. Biol. Med. 150, 106138. [PubMed: 36191393]
36. Rizk J (2021). 4D flow MRI applications in congenital heart disease. Eur. Radiol. 31, 1160–1174. [PubMed: 32870392]
37. Tabrizchi R, and Pugsley MK (2000). Methods of blood flow measurement in the arterial circulatory system. J. Pharmacol. Toxicol. Methods 44, 375–384. [PubMed: 11325580]
38. Sun Z, and Chaichana T (2016). A systematic review of computational fluid dynamics in type B aortic dissection. Int. J. Cardiol. 210, 28–31. [PubMed: 26922709]
39. Berg P, Saalfeld S, Voß S, et al. (2019). A review on the reliability of hemodynamic modeling in intracranial aneurysms: why computational fluid dynamics alone cannot solve the equation. Neurosurg. Focus 47, E15.
40. Saqr KM, Rashad S, Tupin S, et al. (2020). What does computational fluid dynamics tell us about intracranial aneurysms? a meta-analysis and critical review. J. Cerebr. Blood Flow Metabol. 40, 1021–1039.
41. Ong CW, Wee I, Syn N, et al. (2020). Computational fluid dynamics modeling of hemodynamic parameters in the human diseased aorta: A systematic review. Ann. Vasc. Surg. 63, 336–381. [PubMed: 31344467]
42. Pavlin-Premrl D, Boopathy SR, Nemes A, et al. (2021). Computational fluid dynamics in intracranial atherosclerosis-lessons from cardiology: A review of CFD in intracranial atherosclerosis. J. Stroke Cerebrovasc. Dis. 30, 106009. [PubMed: 34343837]
43. Ballout AA, Prochilo G, Kaneko N, et al. (2023). Computational fluid dynamics in intracranial atherosclerotic disease. Stroke: Vascular and Interventional Neurology 4, e000792.
44. Bernabeu MO, Lu Y, Abu-Qamar O, et al. (2018). Estimation of diabetic retinal microaneurysm perfusion parameters based on computational fluid dynamics modeling of adaptive optics scanning laser ophthalmoscopy. Front. Physiol. 9, 989. [PubMed: 30245632]
45. He L, Sampani K, Zheng X, et al. (2020). Predictive modelling of thrombus formation in diabetic retinal microaneurysms. R. Soc. Open Sci. 7, 201102. [PubMed: 32968536]

Author Manuscript Author Manuscript Author Manuscript Author Manuscript

46. Fatma K, Carine G-C, Marine G, et al. (2022). Numerical modeling of residual type B aortic dissection: longitudinal analysis of favorable and unfavorable evolution. Med. Biol. Eng. Comput. 60, 769–783. [PubMed: 35076858]
47. Xiong Z, Yang P, Li D, et al. (2020). A computational fluid dynamics analysis of a patient with acute non-a-non-b aortic dissection after type i hybrid arch repair. Med. Eng. Phys. 77, 43–52. [PubMed: 31948772]
48. Chen D, Müller-Eschner M, Kotelis D, et al. (2013). A longitudinal study of type-B aortic dissection and endovascular repair scenarios: computational analyses. Med. Eng. Phys. 35, 1321–1330. [PubMed: 23523079]
49. Moretti S, Tauro F, Orrico M, et al. (2023). Comparative analysis of patient-specific aortic dissections through computational fluid dynamics suggests increased likelihood of degeneration in partially thrombosed false lumen. Bioengineering 10, 316. [PubMed: 36978707]
50. Zhu Y, Mirsadraee S, Ulrich R, et al. (2022). Fluid-structure interaction simulations of repaired type Aaortic dissection: a comprehensive comparison with rigid wall models. Front. Physiol. 1113.
51. Wang X, Ghayesh MH, Kotousov A, et al. (2023). Fluid–structure interaction study for biomechanics and risk factors in stanford type aortic dissection. Int. J. Numer. Method. Biomed. Eng. 39, e3736. [PubMed: 37258411]
52. Armour C, Guo B, Saitta S, et al. (2024). The role of multiple re-entry tears in type B aortic dissection progression: a longitudinal study using a controlled swine model. J. Endovasc. Ther. 31, 104–114. [PubMed: 35852439]
53. Kim T, van Bakel PAJ, Nama N, et al. (2023). A computational study of dynamic obstruction in type b aortic dissection. J. Biomech. Eng. 145, 031008. [PubMed: 36459144]
54. Raissi M, Perdikaris P, and Karniadakis G (2019). Physics-informed neural networks: A deep learning framework for solving forward and inverse problems involving nonlinear partial differential equations. J. Comput. Phys. 378, 686–707.
55. George EK, Kevrekidis IG, Lu L, et al. (2021). Physics-informed machine learning. Nature Reviews Physics 3, 422–440.
56. Lu L, Meng X, Mao Z, et al. (2021). DeepXDE: A Deep Learning Library for Solving Differential Equations. SIAM Rev. 63, 208–228.
57. Wu W, Daneker M, Jolley MA, et al. (2023). Effective data sampling strategies and boundary condition constraints of physics-informed neural networks for identifying material properties in solid mechanics. Appl. Math. Mech. 44, 1039–1068. [PubMed: 37501681]
58. Zhu M, Zhang H, Jiao A, et al. (2023). Reliable extrapolation of deep neural operators informed by physics or sparse observations. Comput. Methods Appl. Mech. Eng. 412, 116064.
59. Yu J, Lu L, Meng X, et al. (2022). Gradient-enhanced physics-informed neural networks for forward and inverse PDE problems. Comput. Methods Appl. Mech. Eng. 393, 114823.
60. Lu L, Pestourie R, Yao W, et al. (2021). Physics-informed neural networks with hard constraints for inverse design. SIAM J. Sci. Comput. 43, B1105–B1132.
61. Mitchell D, Zhang Z, George EK, et al. (2023). Systems Biology: Identifiability Analysis and Parameter Identification via Systems-Biology-Informed Neural Networks (Springer US), pp. 87–105.
62. Cai S, Li H, Zheng F, et al. (2021). Artificial intelligence velocimetry and microaneurysm-on-a-chip for three-dimensional analysis of blood flow in physiology and disease. Proc. Natl. Acad. Sci. USA 118, e2100697118. [PubMed: 33762307]
63. Jin X, Cai S, Li H, et al. (2021). Nsfnets (navier-stokes flownets): Physics-informed neural networks for the incompressible navier-stokes equations. J. Comput. Phys. 426, 109951.
64. Raissi M, Yazdani A, and Karniadakis GE (2020). Hidden fluid mechanics: Learning velocity and pressure fields from flow visualizations. Science 367, 1026–1030. [PubMed: 32001523]
65. Cai S, Wang Z, Fuest F, et al. (2021). Flow over an espresso cup: inferring 3-D velocity and pressure fields from tomographic background oriented schlieren via physics-informed neural networks. J. Fluid Mech. 915, A102.
66. Boster KAS, Cai S, Ladrón-de-Guevara A, et al. (2023). Artificial intelligence velocimetry reveals in vivo flow rates, pressure gradients, and shear stresses in murine perivascular flows. Proc. Natl. Acad. Sci. USA 120, e2217744120. [PubMed: 36989300]

Author Manuscript Author Manuscript Author Manuscript Author Manuscript

67. Arzani A, Wang J-X, and D'Souza RM (2021). Uncovering near-wall blood flow from sparse data with physics-informed neural networks. Phys. Fluids 33, 071905.
68. Sun L, and Wang J-X (2020). Physics-constrained bayesian neural network for fluid flow reconstruction with sparse and noisy data. Theoretical and Applied Mechanics Letters 10, 161–169.
69. Sun L, Gao H, Pan S, et al. (2020). Surrogate modeling for fluid flows based on physics-constrained deep learning without simulation data. Comput. Methods Appl. Mech. Eng. 361, 112732.
70. Fathi MF, Perez-Raya I, Baghaie A, et al. (2020). Super-resolution and denoising of 4D-flow MRI using physics-informed deep neural nets. Comput. Methods Progr. Biomed. 197, 105729.
71. Barisione C, Charnigo R, Howatt DA, et al. (2006). Rapid dilation of the abdominal aorta during infusion of angiotensin ii detected by noninvasive high-frequency ultrasonography. J. Vasc. Surg. 44, 372–376. [PubMed: 16890871]
72. Phillips EH, Di Achille P, Bersi MR, et al. (2017). Multi-modality imaging enables detailed hemodynamic simulations in dissecting aneurysms in mice. IEEE Trans. Med. Imag. 36, 1297–1305.
73. Ferruzzi J, Bersi MR, and Humphrey JD (2013). Biomechanical phenotyping of central arteries in health and disease: advantages of and methods for murine models. Ann. Biomed. Eng. 41, 1311–1330. [PubMed: 23549898]
74. Dyverfeldt P, Bissell M, Barker AJ, et al. (2015). 4D flow cardiovascular magnetic resonance consensus statement. J. Cardiovasc. Magn. Reson. 17, 72. [PubMed: 26257141]
75. Ngo MT, Kim CI, Jung J, et al. (2019). Four-dimensional flow magnetic resonance imaging for assessment of velocity magnitudes and flow patterns in the human carotid artery bifurcation: Comparison with computational fluid dynamics. Diagnostics 9, 223. [PubMed: 31847224]
76. Rothenberger SM, Zhang J, Brindise MC, et al. (2022). Modeling bias error in 4D flow MRI velocity measurements. IEEE Trans. Med. Imag. 41, 1802–1812.
77. Xu H, Chen Y, and Zhang D (2024). Worth of prior knowledge for enhancing deep learning. Nexus 1, 100003.
78. Bersi MR, Acosta Santamaría VA, Marback K, et al. (2020). Multimodality imaging based characterization of regional material properties in a murine model of aortic dissection. Sci. Rep. 10, 9244. [PubMed: 32514185]
79. Womersley JR (1957). An elastic tube theory of pulse transmission and oscillatory flow in mammalian arteries (Wright Air Development Center). Number 614.
80. Grinberg L, and Karniadakis GE (2008). Outflow boundary conditions for arterial networks with multiple outlets. Ann. Biomed. Eng. 36, 1496–1514. [PubMed: 18612828]
81. Yazdani A, He L, Bersi MR, et al. (2018). Data-driven modeling of hemodynamics and its role on thrombus size and shape in aortic dissections. Sci. Rep. 8, 1–18. [PubMed: 29311619]
82. George EK, and Sherwin S (2005). Spectral/hp Element Methods for Computational Fluid Dynamics (Oxford University Press on Demand).
83. Wang H, Lu L, null SS, et al. (2023). Learning specialized activation functions for physics-informed neural networks. Commun. Comput. Phys. 34, 869–906.

Author Manuscript Author Manuscript Author Manuscript Author Manuscript

BROADER CONTEXT

Aortic dissection (AD) is a life-threatening event responsible for significant morbidity and mortality across diverse age groups. Quantitative assessments of hemodynamics within aneurysmal and dissected aortas have improved the prognosis of AD and aortic aneurysms. In this work, we introduce warm-start PINNs (WS-PINNs), a computational framework leveraging transfer learning, physics modeling, experimental data, and NNs, to address the limitations of existing approaches for hemodynamic analysis. WS-PINNs reduce reliance on extensive measurement data and mitigate dependencies of model prediction accuracy on inflow/outflow boundary conditions, potentially leading to an improved predictive capacity and interventional planning. Moreover, the proposed computational framework has the potential to be utilized to address various other aortic conditions, including artery stenosis and a range of aneurysms. Thus, its impact could extend significantly across diverse medical scenarios.

Author Manuscript Author Manuscript Author Manuscript Author Manuscript

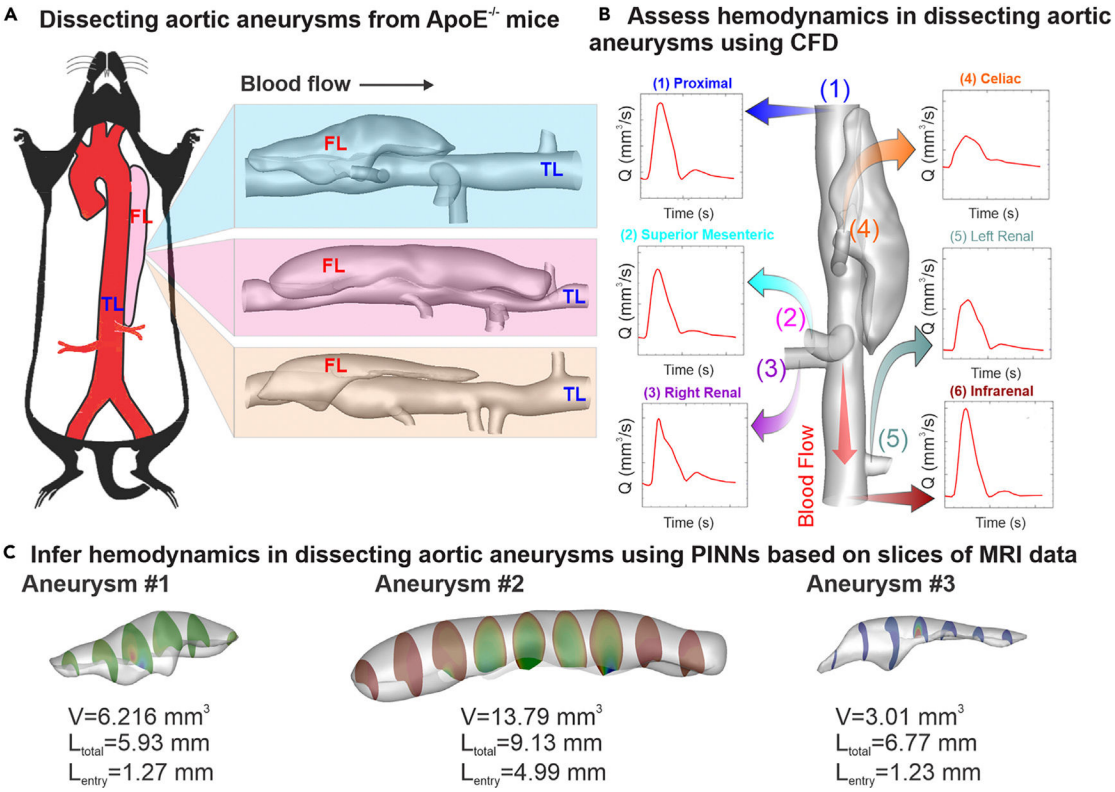

Figure 1. Assessment of hemodynamics in dissecting aortic aneurysms

(A) Three realistic geometries of dissecting aortic aneurysms reconstructed from ApoE$^{-/-}$ mice are employed to examine the accuracy and efficiency of the proposed PINN model.

(B) Assessment of hemodynamics in dissecting aortic aneurysms using a conventional CFD approach requires the knowledge of the flow BCs at all the inlets and outlets as well as the vessel boundaries for aneurysm, aorta, and its different branches.

(C) Assessment of hemodynamics in dissecting aortic aneurysms using PINNs only needs partial information of the flow field provided by MRI or other modalities (i.e., the velocities on the slices highlighted in the figure).

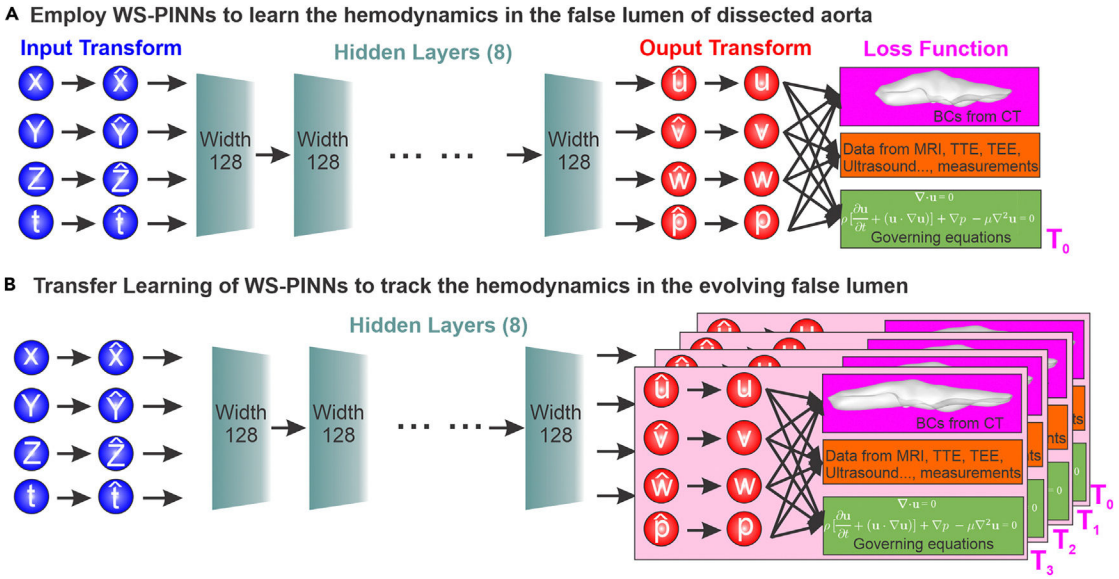

Figure 2. WS-PINNs for inferring the hemodynamics within the FL of the dissected aorta

(A) The proposed model comprises an input layer containing 4 neurons, which read the coordinates, $x, y, z,$ and time t, as the model's inputs. These 4 input quantities are scaled before input into the NNs to facilitate the training process. The proposed model also consists of 8 hidden layers with 128 neurons per layer and 1 output layer to output the velocity components, , v, **and** w, and pressure p. WS-PINNs can integrate the multi-modality data, such as (1) vessel boundaries from CT images (purple box), (2) blood flow measurements from MRI or ultrasound (purple box), with 3 laws of physics (green box) by assimilating this information into the loss function of the NNs for assessing the high-resolution 3D hemodynamics without the knowledge flow BCs.

(B) Transfer learning is performed by refining the existing WS-PINNs model (trained using the initial examination (T_0)) using the newly acquired geometries and measurement data ($T_1 - T_3$).

Author Manuscript Author Manuscript Author Manuscript Author Manuscript

Author Manuscript Author Manuscript Author Manuscript Author Manuscript

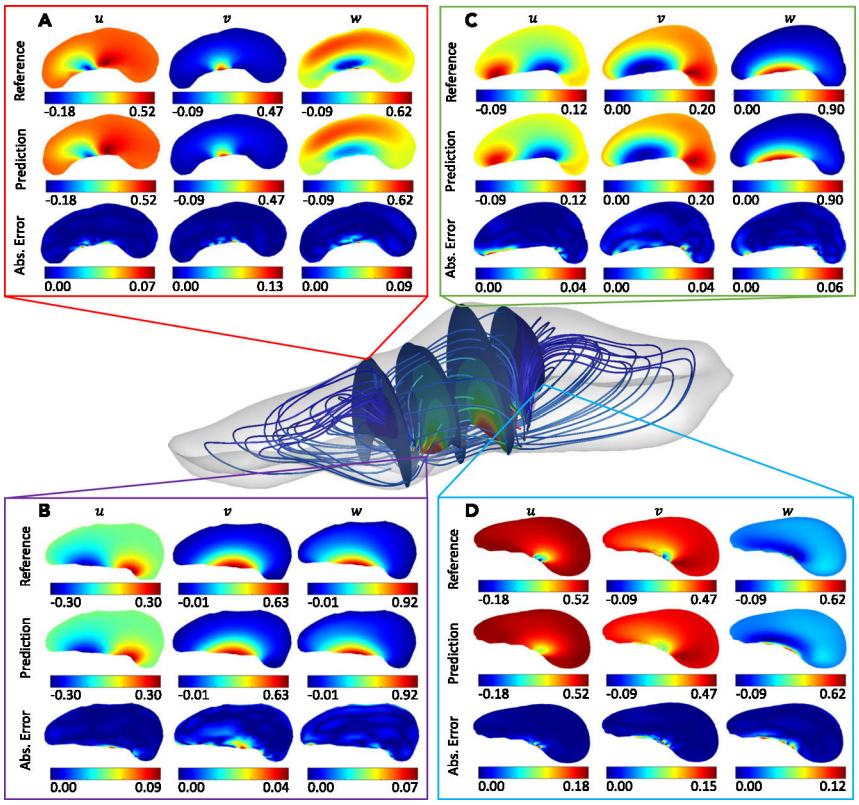

Figure 3. 3D velocity field in aneurysm 1 predicted by the proposed WS-PINNs model

The streamline of the blood flow within the aneurysm is illustrated. (A–D) Four randomly selected cross-sections are selected for comparison between the model prediction and CFD simulations on the 3 velocity components. w represents the velocity component along the longitudinal flow direction along the aorta, while u and v represent the flow direction within the cross-section of the planes perpendicular to the aorta.

Author Manuscript Author Manuscript Author Manuscript Author Manuscript

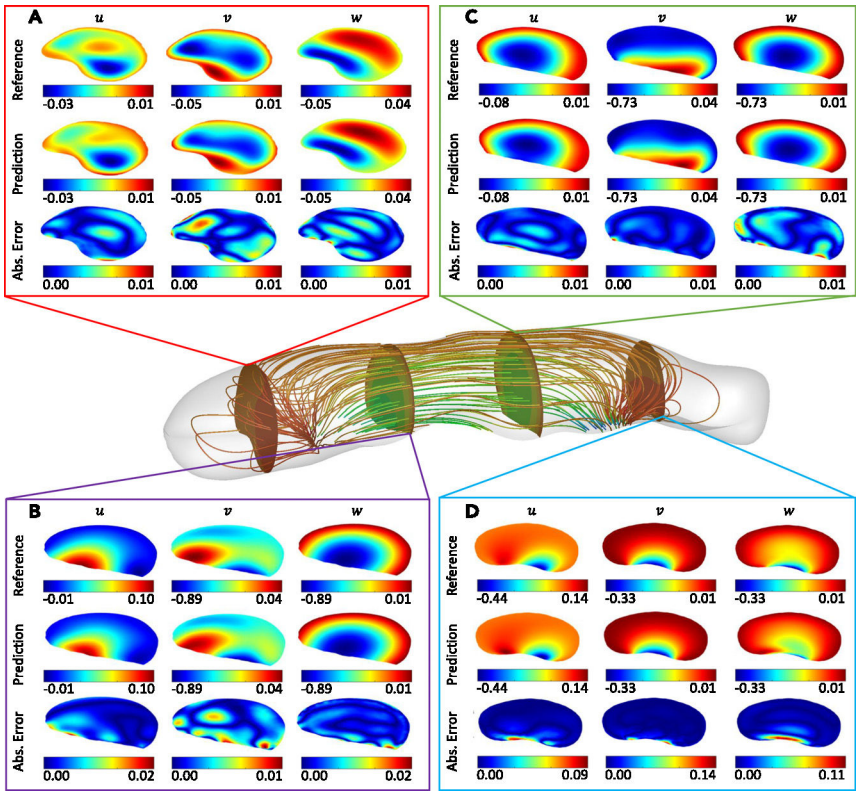

Figure 4. 3D velocity field in aneurysm 2 predicted by the proposed WS-PINNs model

The streamline of the blood flow within the aneurysm is illustrated. (A–D) Four randomly selected cross-sections are selected for comparison between the model prediction and CFD simulations on the 3 velocity components.

Author Manuscript Author Manuscript Author Manuscript Author Manuscript

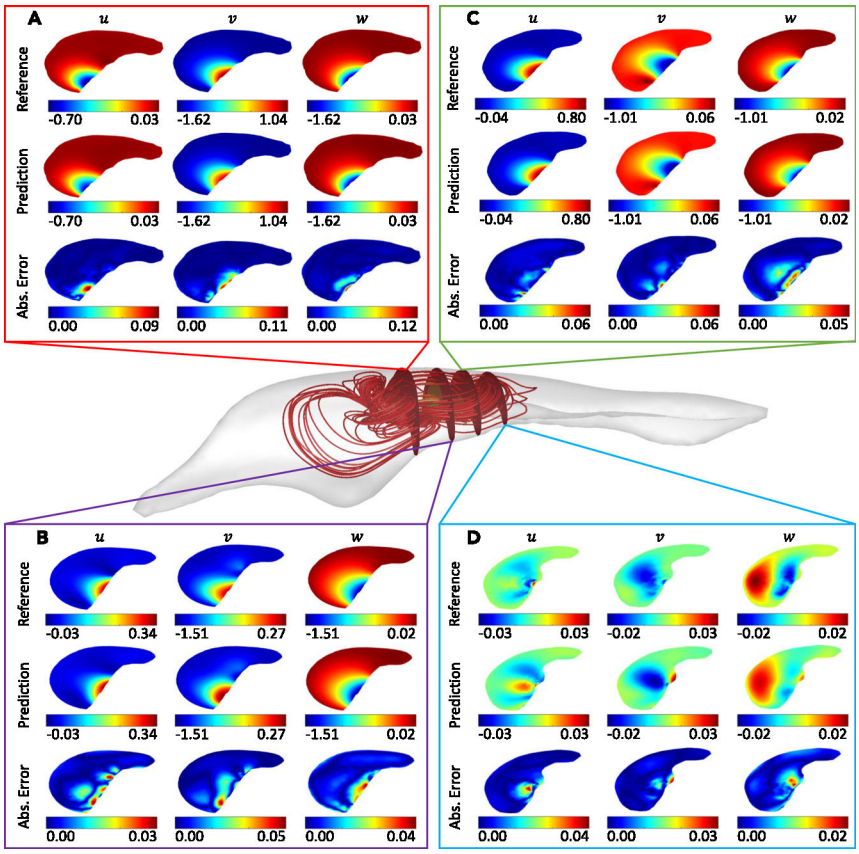

Figure 5. 3D velocity field in aneurysm 3 predicted by the proposed WS-PINNs model

The streamline of the blood flow within the aneurysm is illustrated. (A–D) Four randomly selected cross-sections are selected for comparison between the model prediction and CFD simulations on the 3 velocity components.

Author Manuscript Author Manuscript Author Manuscript Author Manuscript

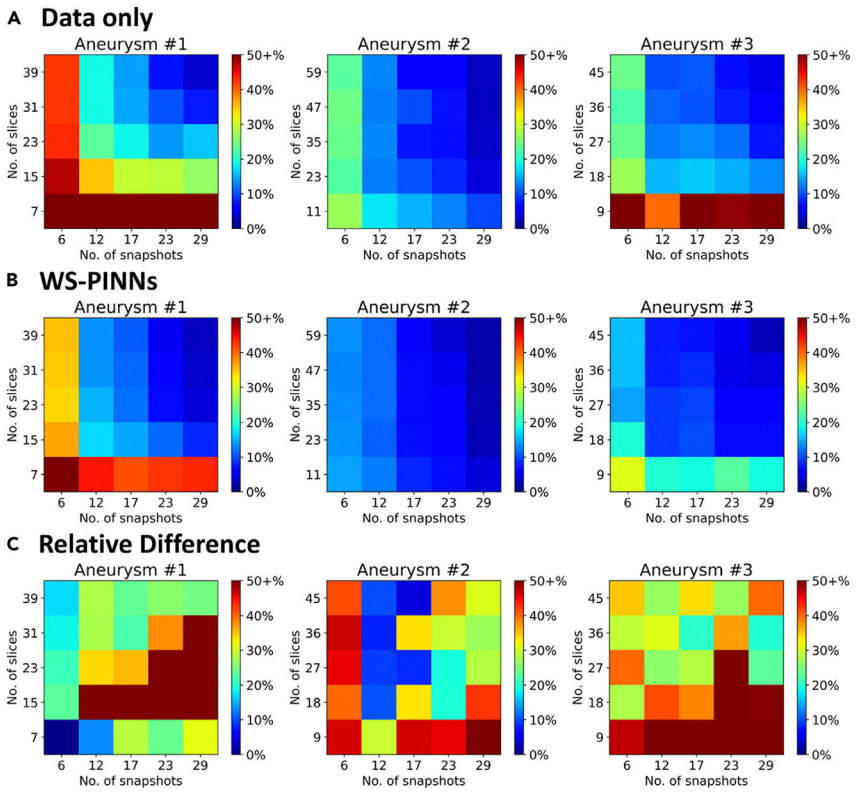

Figure 6. Performance of NN and WS-PINNs using synthetic MRI data with various spatial and temporal resolutions

(A and B) L_2 relative error of the examined aneurysms 1–3, (A) when only measurement data are used for training the NNs, and (B) when both data and the laws of physics are considered for training the WS-PINNs.

(C) Relative percentage decrease in L_2 relative error (see Equation 1) with the inclusion of physics compared to the data-drive approach. The x-axis denotes the number of snapshots extracted from 1 cardiac cycle for training the model, while the y-axis represents the number of slices of synthetic MRI data used for training. The color highlights the magnitude of prediction errors.

Author Manuscript Author Manuscript Author Manuscript Author Manuscript

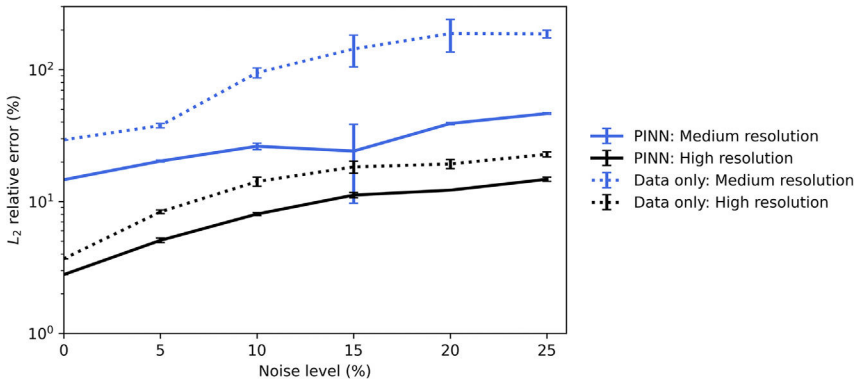

Figure 7. Noise effect on L_2 relative error

We consider the effect of noise on the L_2 relative error in aneurysm 1 for high and medium resolutions in data only and WS-PINNs models. Noise is white Gaussian noise, and the noise level is measured with respect to the maximum velocity. Error bars are SDs from 3 trials, except for 0 noise levels, where only 1 trial is used.

Author Manuscript Author Manuscript Author Manuscript Author Manuscript

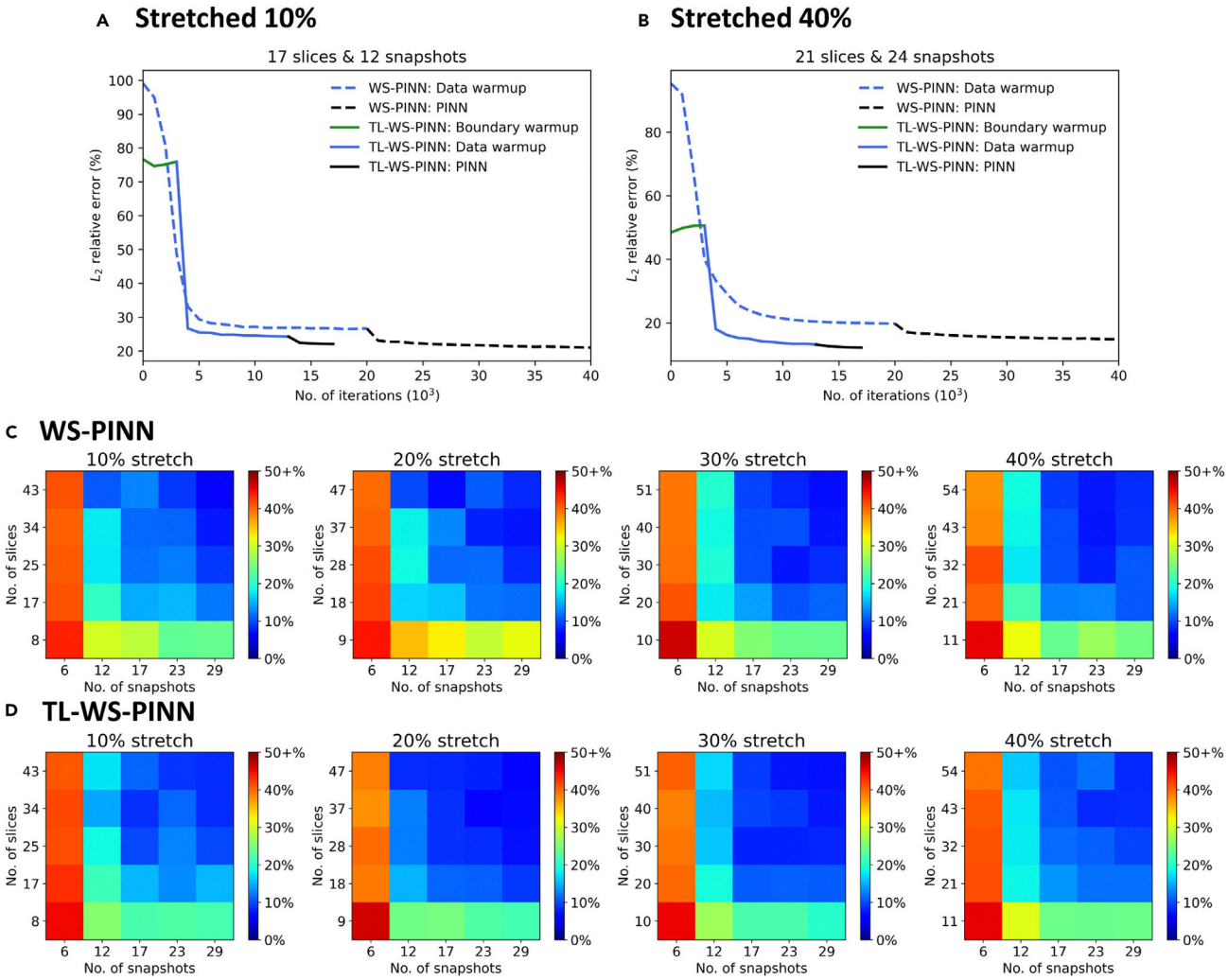

Figure 8. L_2 relative error of WS-PINNs and transfer learning-WS-PINNs

(A and B) Transfer learning-WS-PINNs (solid lines) significantly reduce the training time by reducing the number of iterations required for training. With the advent of boundary warm-up (green lines) in transfer learning, the data warm-up (blue lines) and PINN stage (black lines) converge much more quickly, as opposed to WS-PINNs (dotted lines), leading to faster convergence, with examples provided for (A) the 10% stretched case and (B) the 40% stretched case.

(C and D) While using transfer learning reduces the training time of our WS-PINNs models by approximately 50%, the accuracy of model predictions is sustained. The L_2 relative error is approximately the same for multiple resolutions and stretching cases for both models, indicating no major negatives in using the proposed transfer learning-WS-PINNs.

Author Manuscript Author Manuscript Author Manuscript Author Manuscript

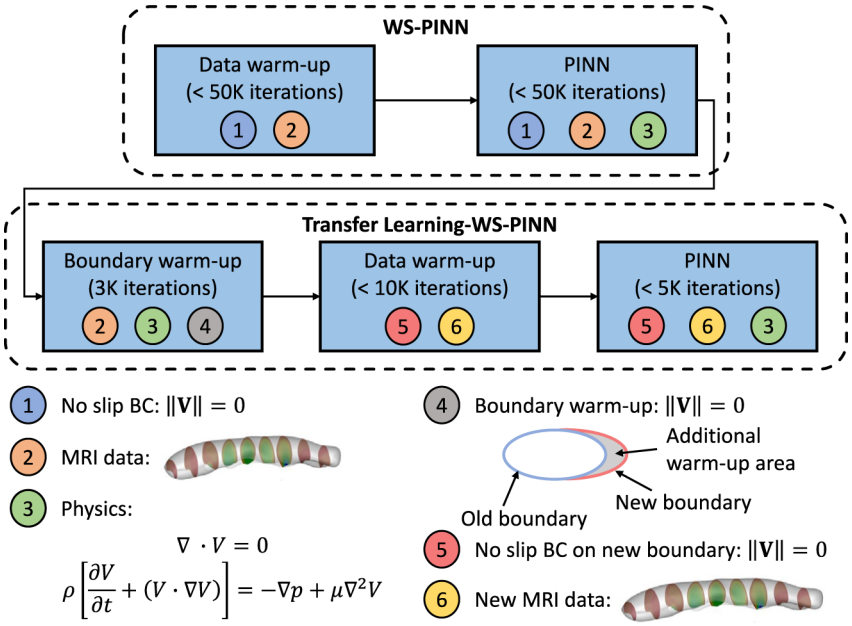

Figure 9. The workflow for utilizing WS-PINNs and transfer learning-WS-PINNs

The training of WS-PINNs is completed via a data warm-up step, followed by adding the physics constraints. These steps take fewer than 50,000 iterations to complete and produce a model with the error reported in Figure 6B. The trained WS-PINNs model can be used in transfer learning via a boundary warm-up step by using the new boundary of the evolved FL with old flow data for 3,000 iterations, followed by a data warm-up with the new data and new boundary for, at most, 10,000 iterations. The training is completed by adding the physical constraints for another 5,000 iterations.